

Hyperparameter Optimization and Force Error Correction of Neuroevolution Potential for Predicting Thermal Conductivity of Wurtzite GaN

Zhuo Chen^{1,2}, Yuejin Yuan¹, Wenyang Ding³, Shouhang Li⁴, Meng An^{3*}, Gang Zhang^{2*},

¹College of Mechanical and Electrical Engineering, Shaanxi University of Science and Technology, Xi'an, Shaanxi 710049, China

²Yangtze Delta Region, Academy of Beijing Institute of Technology, JiaXing, Zhejiang, China

³Department of Mechanical Engineering, The University of Tokyo, 7-3-1 Hongo, Bunkyo, Tokyo 113-8656, Japan.

⁴Centre de Nanosciences et de Nanotechnologies, CNRS, Université Paris-Saclay, 10 Boulevard Thomas Gobert, 91120 Palaiseau, France

Corresponding author:

anmeng@photon.t.u-tokyo.ac.jp (M. A.)

gangzhang2006@gmail.com (G. Z.)

Abstract

As a representative of wide-bandgap semiconductors, wurtzite gallium nitride (GaN) has been widely utilized in high-power devices due to high breakdown voltage and low specific on-resistance. Accurate prediction of wurtzite GaN thermal conductivity is a prerequisite for designing effective thermal management systems of electronic applications. Machine learning-driven molecular dynamics simulation offers a promising approach to predicting the thermal conductivity of large-scale systems without requiring predefined parameters. However, these methods often underestimate the thermal conductivity of materials with inherently high thermal conductivity due to the large predicted force error compared with first-principle calculation, posing a critical challenge for their broader application. In this study, we successfully developed a neuroevolution potential for wurtzite GaN and accurately predicted its thermal conductivity, 259 ± 6 W/m-K at room temperature, achieving excellent agreement with reported experimental measurements. The hyperparameters of neuroevolution potential (NEP) were optimized based on systematic analysis of reproduced energy and force, structural feature, computational efficiency. Furthermore, a force prediction error correction method was implemented, effectively reducing the error caused by the additional force noise in the Langevin thermostat by extrapolating to the zero-force error limit. This study provides valuable insights and holds significant implication for advancing efficient thermal management technologies in wide-bandgap semiconductor devices.

Keywords: Gallium nitride, Molecular dynamics, Thermal conductivity, Machine learning potential

1. Introduction

The wide-bandgap semiconductors, exemplified by GaN and SiC, have been widely utilized in high-power devices due to high breakdown voltage and low specific on-resistance¹. However, these high-power devices often operate under extreme conditions, such as high temperatures, high voltages, and high-frequency environments². These conditions typically result in extremely high heat flux densities, which can adversely impact the devices' stability and operation lifespan^{3,4}. Accurate prediction and characterization of the thermal conductivity of wurtzite GaN are essential for understanding its thermal transport mechanisms and designing efficient thermal management systems.

Over the past decades, extensive studies have focused on the prediction and characterization of the thermal conductivity of wurtzite GaN using both theoretical methods^{5,6,7} and experimental measurements^{8,9,10}. The measured thermal conductivity of wurtzite GaN typically has not reached a consistent conclusion, generally ranging from 180 to 220 W/m-K. This variability arises from differences in experimental samples, measurement methods, and the limited availability of single-crystalline wurtzite GaN samples. Recently, the development of a high-purity wurtzite GaN sample has enabled the measurement of thermal conductivity up to 246 W/m-K through systematic experimental characterization¹¹. In contrast, first-principle calculation-based Boltzmann transport equation tends to overestimate the thermal conductivity of wurtzite GaN using the local-density approximation (LDA) form of the exchange-correlation function, primarily inconsistent lattice parameters with experimental samples and simplified anharmonicity calculations^{5,12}. In contrast, our previous work¹³ determined the thermal conductivity of wurtzite GaN to be 264 W/m-K, employing the PBE form of the exchange-correlation function while maintaining consistent lattice parameters ($a = 3.184 \text{ \AA}$ and $c = 5.187 \text{ \AA}$). This result aligns well with experimental measurement¹¹. Similarly, molecular dynamics (MD) simulations using empirical potential predicted a thermal conductivity of approximately 180 W/m-K^{14,15}, which is significantly lower than the reported experimental value¹¹. Machine learning-driven molecular dynamics simulation offers a promising alternative for predicting the thermal conductivity of large-scale systems without the need of predefined parameters. However, these methods often underestimate the thermal conductivity of materials with inherently high thermal conductivity^{16,17}, such as wurtzite GaN, posing a critical challenge for their broader application.

In this work, we first developed the neuroevolution potential (NEP)¹⁸ for wurtzite GaN, a representative of machine learning potential (MLP) that combines high computational efficiency with excellent accuracy. We systematically investigated the influence of NEP

hyperparameters on the accuracy of thermal conductivity prediction and computational efficiency. Furthermore, we implemented a correction method to eliminate force prediction errors in the Langevin thermostat¹⁹, achieving an accurate thermal conductivity of 259 ± 6 W/m-K at room temperature, which aligns closely with experimental value¹¹.

2. Methods

2.1 Neuroevolution potential training

In NEP mode, the radial and angular components are influenced by the cutoff radii of r_c^R and r_c^A , respectively. In our study, two cutoff radii of r_c^R and r_c^A were checked for optimize the accuracy of NEP model including the value of 4.5 Å, 5.0 Å and 5.5 Å. We performed tests to determine an optimal cutoff value, other hyperparameters used to train the NEP model are listed in Table S1. In total, we gathered 404 structures for the training set and 180 structures for the testing set. The training set includes an unitcell, a supercell, 200 MD structures at temperatures ranging from 100 to 1900 K, and 202 structures with tiny random atomic displacements and variations in lattice constants. We employed a general-purpose machine learning model, MACE-MP²⁰, in conjunction with the *Atomic Simulation Environment* (ASE) package²¹ to perform MD simulations using the canonical (NVT) ensemble. The testing set was generated by performing MD simulations of heating from 100 to 1900 K using the NEP model, which was trained on the training set. Static calculations based on the first-principles method were performed to determine obtain the energy, atomic forces and virials of each structure.

2.2 DFT calculations for reference data generation

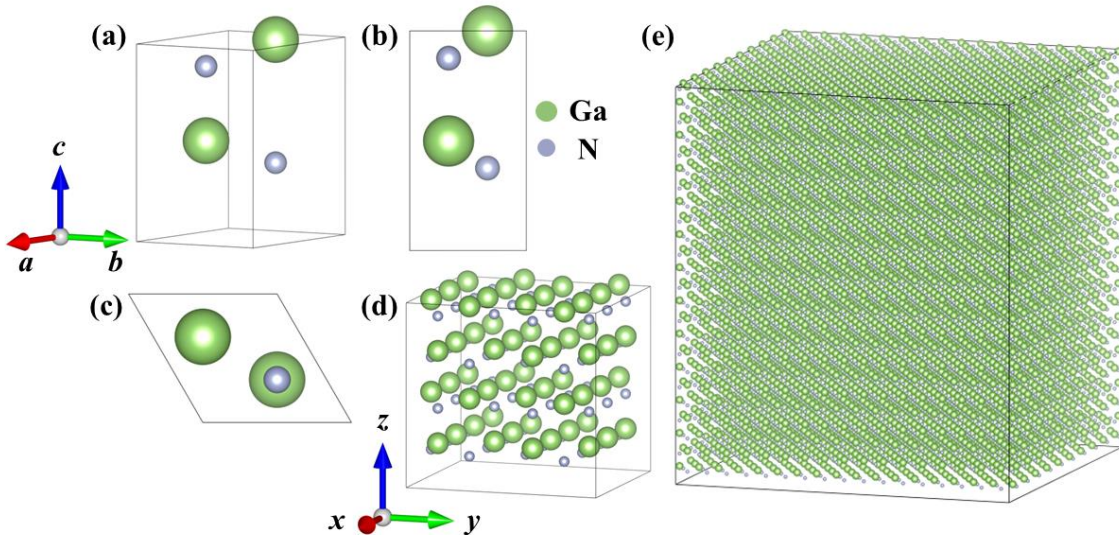


Figure 1. The snapshots of (a)-(c) the unitcell of wurtzite GaN, (d) the supercell for MACE-MP-based MD simulations, and (e) the supercell for thermal conductivity calculations.

First-principles calculations were performed using density function theory (DFT) as implemented in the *Vienna Ab Initio Simulation Package* (VASP)²². The unitcell of wurtzite GaN, as shown in **Figure 1(a-c)**, with a hexagonal system and the $P6_3mc$ space group. The converged lattice constants of wurtzite GaN to be $a = b = 3.219 \text{ \AA}$ and $c = 5.243 \text{ \AA}$, which are approximately 1% larger than the experimental values ($a = 3.19 \text{ \AA}$ and $c = 5.189 \text{ \AA}$). This discrepancy is attributed to the PBE functional²³, which tends to overestimate lattice constants. In order to eliminate artificial factor, original lattice constants are not considered adjusted in this work. The hexagonal system was converted to a cubic lattice (**Figure 1(d)**) with dimensions $9.65 \text{ \AA} \times 11.153 \text{ \AA} \times 10.487 \text{ \AA}$ for MD simulations used to build datasets. Structural visualization was carried out using the VESTA package²⁴.

2.3 MD simulations

All MD simulations for thermal conductivity calculations were performed at 300 K using the GPUMD package²⁵ (version 3.9.4) with the NEP models (version 4)²⁶. The simulation process involved three distinct runs, each with a time step of 1 fs. The first run, lasting 0.5 ns, employed a stochastic cell rescaling (SCR) thermostat²⁷ within the isothermal-isobaric (NPT) ensemble, with a target pressure of zero. The second run, conducted for 0.2 ns, used a Bussi-Donadio-Parrinello (BDP) thermostat²⁸ in the NVT ensemble. Finally, a 15 ns simulation was performed in the NVT ensemble, during which the running thermal conductivity was recorded. We only considered the thermal conductivity of wurtzite GaN along z -direction. The thermal conductivity was calculated using the homogeneous non-equilibrium molecular dynamics (HNEMD) method²⁹, which is unique to GPUMD. In this method, the heat current is proportional to the magnitude of the driving force parameter F_e , cautious selection of F_e is essential to secure a large signal-to-noise ratio within the linear-response regime of the systems.

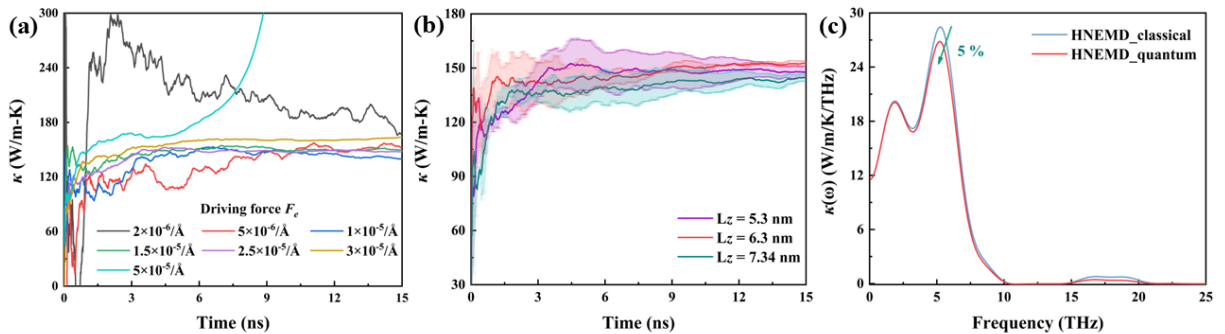


Figure 2. (a) Cumulative average of the thermal conductivity of wurtzite GaN at 300 K and zero pressure. The driving force parameter F_e listed in the legend ranges from 2×10^{-6} to $5 \times 10^{-3} \text{ \AA}^{-1}$. (b) Cumulative average of the thermal conductivity of wurtzite GaN at 300 K and zero pressure. The length of z -direction increases from 5.3 nm to 7.34 nm, three independent runs

are performed. (c) The classical and quantum-corrected spectral thermal conductivity of wurtzite GaN at 300 K. The green arrow and number indicate the overvalued part of the classical MD.

To determine the parameter, we conducted extensive tests, the result is presented in **Figure 2(a)**. The system deviates from the linear-response regime when $F_e \geq 5 \times 10^{-5} / \text{\AA}$, while a small value of $F_e = 2 \times 10^{-6} / \text{\AA}$ induces large fluctuations in thermal conductivity. Based on these observations, a value of $F_e = 2.5 \times 10^{-5} / \text{\AA}$ was selected. Additionally, a sufficiently large simulation cell was used to eliminate finite-size effects. As shown in **Figure 2(b)**, we only considered the thermal conductivity of wurtzite GaN in the z -direction in this work, using a simulation cell with dimensions $L_x \times L_y \times L_z = 55.88 \text{\AA} \times 54.83 \text{\AA} \times 63.08 \text{\AA}$ (depicted in **Figure 1(e)**), which containing 16320 atoms. In the classical MD simulations, vibrational modes follow the Maxwell-Boltzmann statistics, meaning each mode contributes to the heat capacity. However, in the quantum statistical mechanics, only the vibrational modes with the frequencies below the cutoff $k_B T \leq \hbar \omega_0$, where ω_0 is the vibrational frequency, contribute to the heat capacity, as described by Bose-Einstein statistics. To investigate the quantum effect, we employ a feasible quantum correction method based on spectral thermal conductivity is available within the HNEMD formalism³⁰:

$$\kappa^q(\omega, T) = \kappa(\omega, T) \frac{x^2 e^x}{(e^x - 1)^2}, \quad (1)$$

$$\kappa^q(T) = \int_0^\infty \frac{d\omega}{2\pi} \kappa^q(\omega, T). \quad (2)$$

where $x = \hbar \omega / k_B T$, \hbar is the reduced Plank constant and k_B is the Boltzmann constant. $\kappa(\omega, T)$ is the classical spectral thermal conductivity and the total quantum corrected thermal conductivity $\kappa^q(T)$ is obtained as an integral of $\kappa^q(\omega, T)$ over the vibrational frequency. The quantum corrected spectral thermal conductivity at 300 K is presented in **Figure 2(c)**, we found that the thermal conductivity decreased by only 5% after quantum correction. This minimal change is attributed to the thermal conductivity of wurtzite GaN is primarily governed by low-frequency (<10 THz) phonons, which exhibit a weak quantum effect. As a result, quantum effect is not considered in the subsequent calculations.

3. Results and Discussion

3.1 Hyperparameter optimization of neuroevolution potential

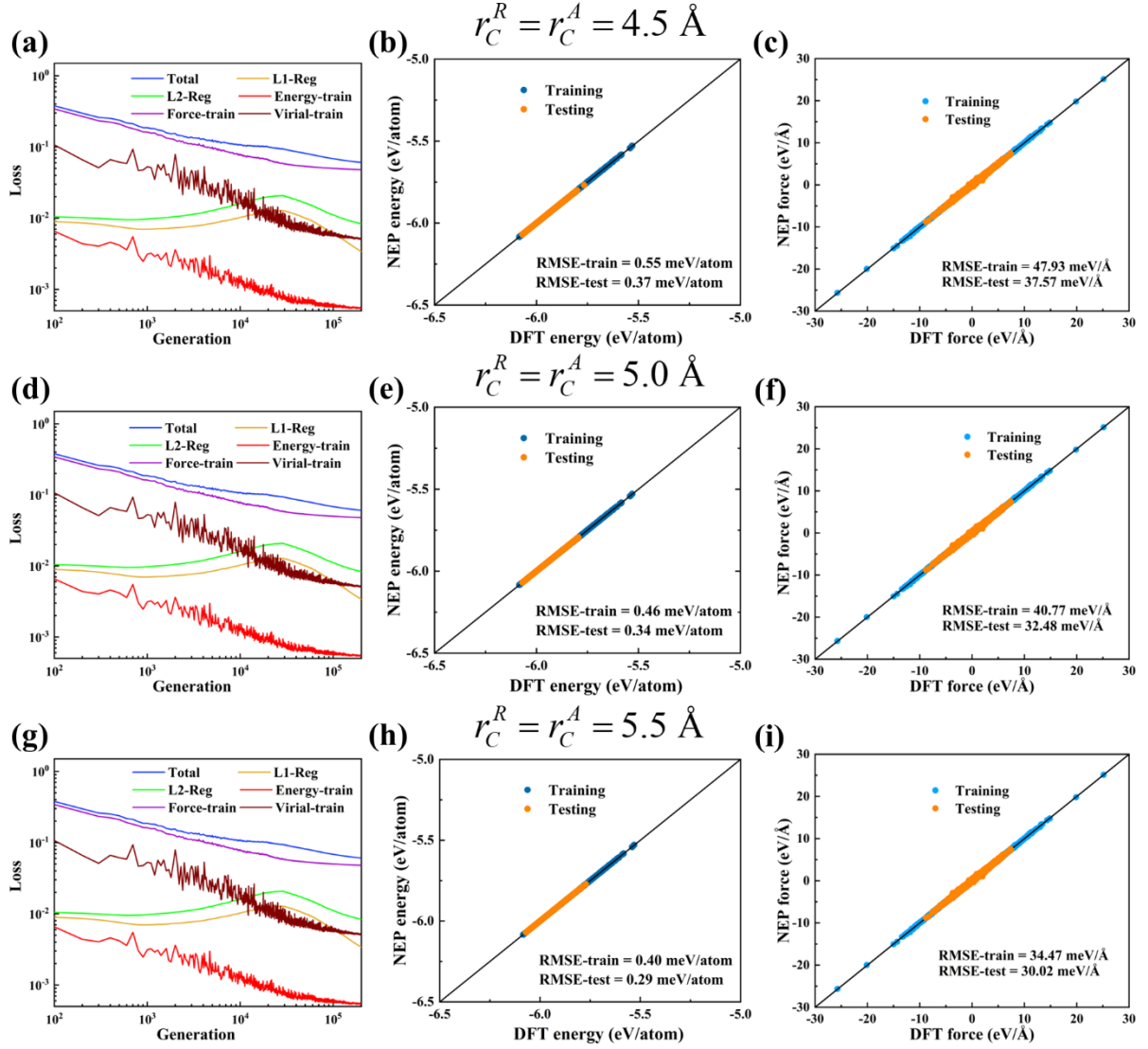


Figure 3. Evolution of the various terms in the loss function, including those for the L1 and L2 regularization, the energy RMSE (eV/atom), force RMSE (eV/Å) and virial RMSE (eV/atom) as a function of the training generation of (a) 4.5 Å, (d) 5.0 Å, and (g) 5.5 Å. Energy calculated from the NEP model as L1 compared to the DFT reference data of (b) 4.5 Å, (e) 5.0 Å, and (h) 5.5 Å. Force calculated from the NEP model as compared to the DFT reference data of (c) 4.5 Å, (f) 5.0 Å, and (i) 5.5 Å. The overall converged training and testing RMSEs of energy and force are presented. Integrated cutoff values are indicated in above of each panel.

The NEP model is a MLP, based on the feedforward neural network and employed to describe the interatomic interaction. In a neural network potential, increasing the number of neurons generally improves the accuracy until convergence. Therefore, the hyperparameters such as the number of radial and angular descriptor components related to the number of neurons, often follow standard values. In MD simulations, when calculating short-range interactions, it is typically sufficient to account only for the contributions of particles within a

cutoff distance. The introduction of truncation approximation greatly reduces the computational cost of interatomic interactions. However, the relationship between the accuracy and truncation of MLP is not monotonic, and there is usually an optimal cutoff that achieves the optimized training accuracy. Our calculations found that the NEP with the highest accuracy was associated with a significantly slower computational speed. Therefore, we question whether a greater cutoff radius is necessary to achieve higher accuracy. In previous study, the cutoff value was determined only after the accuracy test had been conducted³¹. In this work, we hope to do more comprehensive testing to determine a more reasonable cutoff value, which is very meaningful for the training process of standardizing NEP.

Figure 3 presents the training results of three NEP models with different cutoffs, including the radial (r_c^R) and angular (r_c^A) cutoffs. As depicted in **Figure 3(a)(d)(g)**, the loss curve plateaus as the number of training steps increases. The diagonal plots show the errors between the energy and force predicted by the NEP models and DFT calculations. The RMSEs for energy in the training set reveal a decreasing trend as the cutoff radius increases: 0.55 meV/atom for $r_c^R = r_c^A = 4.5$ Å, 0.46 meV/atom for $r_c^R = r_c^A = 5.0$ Å, and 0.40 meV/atom for $r_c^R = r_c^A = 5.5$ Å. Similarly, the force RMSEs demonstrate a consistent improvement with increasing cutoff radii, decreasing from 47.93 meV/Å for $r_c^R = r_c^A = 4.5$ Å, 40.77 meV/Å for $r_c^R = r_c^A = 4.5$ Å, and 34.47 meV/Å for $r_c^R = r_c^A = 4.5$ Å. These results indicate that enlarging the cutoff radius significantly enhances the accuracy of NEP model for capturing both energy and force of DFT calculation due to better representation of longer-range atomic interactions. Upon the optimization of energy and force in NEP, we then evaluated the predictive structure information of wurtzite GaN using the NEPs. All atomic structures were relaxed for 0.5 ns at 300 K using a SCR thermostat in the NPT ensemble, followed by 0.2 ns at 300 K using a BDP thermostat in the NVT ensemble. The radial distribution function (RDF) $g(r)$ and the structural factor (SF) $S(q)$ are shown in **Figure 4(a-b)**. SF highlights the long-range order characteristic of crystalline materials. Interestingly, the structural features remain consistent across different cutoff radii, indicating that a cutoff radii of 4.5 Å or larger is sufficient to accurately capture and construct the crystalline structure of wurtzite GaN.

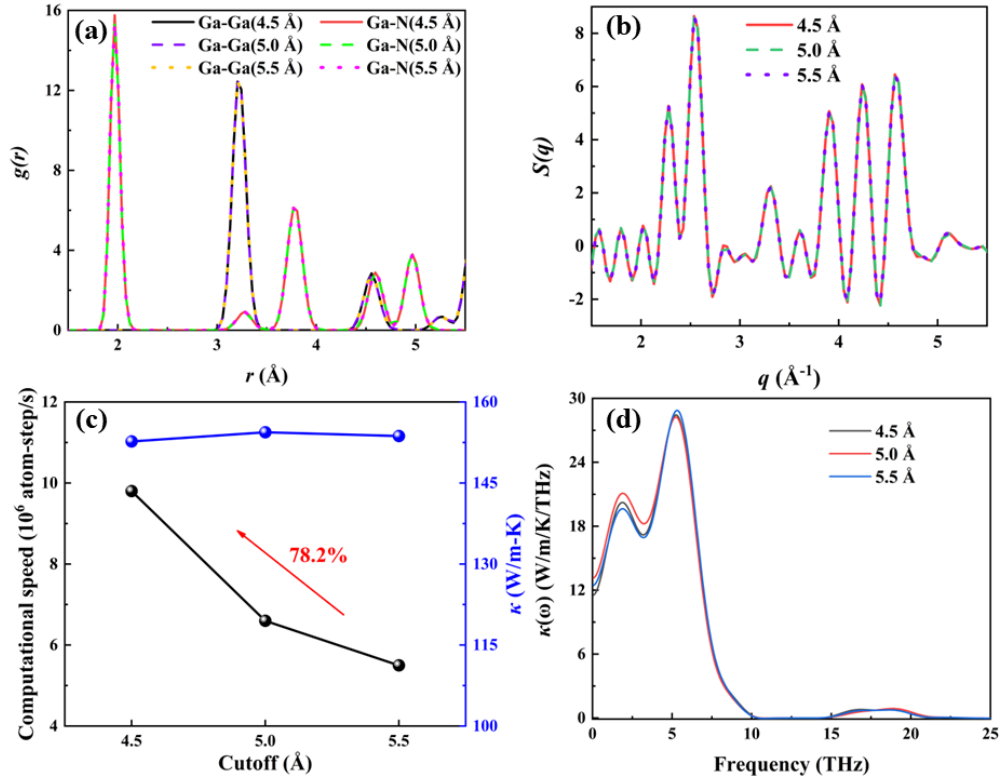


Figure 4. (a) Radial distribution function $g(r)$ of Ga-Ga and Ga-N predicted by NEPs with various cutoff radii. (b) The structure factors $S(q)$ of wurtzite GaN. (c) The computational speed (black axis) of NEPs and the thermal conductivities (blue axis) of wurtzite GaN predicted by NEPs with various cutoff radii. (d) The spectral thermal conductivities predicted by NEPs with various cutoff radii.

In addition to evaluating the structure features using the NEP models, the computational efficiency and accuracy of predicting the thermal conductivity of wurtzite GaN are equally critical. The thermal conductivity of wurtzite GaN along the z -direction was calculated using NEPs with varied cutoff radii, as shown in **Figure 4(c)**. Notably, the thermal conductivity of wurtzite GaN remain consistent with differences of less than 2 W/m-K across three cutoff radii. In contrast, the computational speed with a cutoff radius of 4.5 Å is about 9.8×10^6 atom-step per second on a single Tesla A800 GPU, which is 78.2% faster compared to that with a cutoff radius of 5.5 Å. This significant improvement in computational efficiency highlights the advantage of adopting a smaller cutoff radius, which substantially reduces computational cost and time while maintaining accuracy in structural and thermal conductivity predictions. Furthermore, the spectral thermal conductivity obtained with varying cutoff radii shows consistent results across the entire range of phonon frequencies, as illustrated in **Figure 4(d)**. Based on the above systematic analysis of the reproduced energy and force, structure features,

thermal conductivity predictions, computational efficiency and spectral thermal conductivity from NEPs with varying cutoff radii, a cutoff radius of 4.5 Å was selected to for subsequent thermal conductivity calculations, ensuring a balance between computational efficiency and accuracy.

3.2 Correction of wurtzite GaN thermal conductivity

Despite extensive parameter optimization of the NEP models, the calculated thermal conductivity of wurtzite GaN at 300 K was around 150 W/m-K, which is significantly lower than the 246 W/m-K reported in experimental result¹¹ and the 260 W/m-K in DFT results^{7,32}. Previous studies have highlighted the general tendency of MLPs to underestimate thermal conductivity, particularly in materials with inherently high thermal conductivity^{16,17}. To address this limitation, researchers have developed correction method to reconcile the discrepancies between predicted and experimentally measured thermal conductivity^{33,34}. In this study, we adopted the developed correction method to achieve a more accurate prediction of thermal conductivity of wurtzite GaN.

The core of correction method lies in accounting for an additional force error, which follows a Gaussian distribution in the Langevin thermostat. This approach is analogous to the prediction error of forces observed in the NEP models, providing a systematic way to address discrepancies and enhance the accuracy of thermal conductivity prediction based on MLPs. This is because the Langevin thermostat does not directly regulate the dynamics state of the entire system, as a global thermostat like BDP thermostat does. Instead, it introduces random forces of white noise to influence the dynamics of system, resulting in an additional force error compared to a global thermostat. The magnitude of force error through the Langevin thermostat can be adjusted by the coupling time³³:

$$\sigma_L^2 = \frac{2k_B T m_{ave}}{\tau \Delta t}. \quad (3)$$

where m_{ave} is the average atom mass, k_B is the Boltzmann constant, T is the temperature in the system. τ is the coupling time and Δt is the time step. The total force error σ_{total} can be denoted as $\sigma_{total} = \sqrt{\sigma_{nep}^2 + \sigma_L^2}$, where σ_{nep} is the RMSE of force prediction for the NEP model at the target temperature. The predicted thermal conductivity is directly proportional to σ_{total} , decreasing as σ_{total} increases. Based on a first-order approximation and Matthiessen's rule, the corrected thermal conductivity κ_0 can be calculated using the following formula³³:

$$\kappa_0 = \frac{1}{\frac{1}{\kappa} + \lambda \sigma_{\text{total}}} \quad (4)$$

where κ is the wurtzite GaN thermal conductivity by NEP-HNEMD with the langevin thermostat, λ is a fitting parameter.

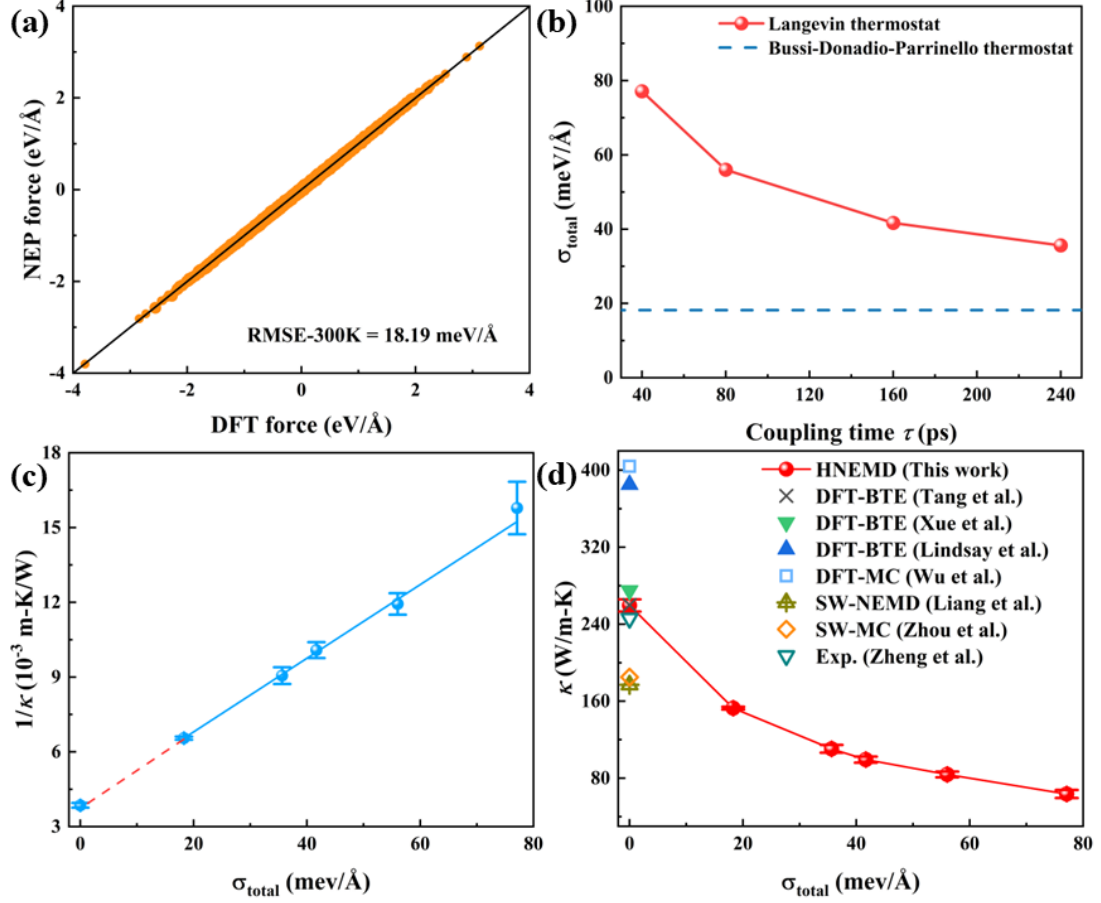


Figure 5. (a) Force prediction of wurtzite GaN at 300 K from the NEP model compared with the DFT reference data. (b) Dependence of total force error σ_{total} on the coupling time. Red dots represents σ_{total} using the Langevin thermostat while blue dotted line represents σ_{total} from the BDP thermostat, which remains unaffected by the coupling time. (c) Inverse thermal conductivity ($1/\kappa$) from NEP-MD simulations as a function of σ_{total} . The solid line represents linear fits, and the red dotted line is an extrapolation of the results. The intersection points at $\sigma_{\text{total}} = 0$ corresponds to the corrected thermal conductivity. (d) Calculated thermal conductivity as a function of σ_{total} . For comparison, DFT values^{5,7,12,32}, SW results^{14,15}, and experimental data¹¹ of thermal conductivity of wurtzite GaN at 300 K are also shown.

We first evaluated the force prediction error of NEP in the MD-simulated structures at 300 K by comparing it to DFT reference data. These atomic configuration structures were generated through NEP-MD simulations using an SCR thermostat at 300 K, with 50 configurations uniformly sampled from 1 ns trajectory for DFT static calculations. **Figure 5(a)** shows the σ_{nep} at 300 K, which can be considered as $\sigma_{\text{total}} = \sigma_{\text{nep}} = 18.19 \text{ meV/\AA}$ when using the BDP thermostat. Notably, the force prediction error of NEP model at 300K in **Figure 5(a)** is significantly lower than the overall force prediction error in **Figure 3(c)**. This is because the training set also includes high-temperature and perturbed structures, which are typically more force-intensive and require the model to predict the temperature-specific error accurately. Subsequently, we examined the force prediction error induced by the additional random force in Langevin thermostat by varying the coupling times to 240, 160, 80, and 40 ps.

Figure 5(b) illustrates the dependence of σ_{total} on the coupling times of the Langevin thermostat, while κ_0 is determined in **Figure 5(c)** by fitting the data using Eq. (4). Using the fitted linear parameter, the thermal conductivity of wurtzite GaN was obtained by extrapolating to $\sigma_{\text{total}} = 0$. The uncorrected and corrected thermal conductivity of wurtzite GaN, obtained from NEP-MD simulations along with experimental data, DFT results, and SW-MD simulations results were presented in **Figure 5(d)**. The calculated thermal conductivities of pure wurtzite GaN from Lindsay et al.⁵ and Wu et al.¹² are significantly higher than experimental value¹¹ due to the difference of lattice constant in wurtzite GaN. The uncorrected thermal conductivities are consistently lower than the other results due to the presence of force prediction errors in the NEP-MD calculations. Interestingly, the corrected thermal conductivity of wurtzite GaN from NEP-MD simulations is $259 \pm 6 \text{ W/m-K}$, which aligns well with the experimental value of 246 W/m-K . The slight overestimation in our results may be attributed to the weak quantum effect at room temperature. Overall, we have achieved an accurate prediction of the pure wurtzite GaN thermal conductivity based on NEP-MD simulations. This work broadens the applicability of force error correction method to a wider range of materials. Furthermore, our finding confirms that wurtzite GaN does not exhibit significant isotopic effects, in contrast to earlier theoretical works.

4. Conclusions

In conclusion, we successfully developed a neuroevolution potential for wurtzite GaN and accurately predicted its thermal conductivity, achieving excellent agreement with reported experimental measurements. This work effectively addresses the common underestimate issue

associated with high thermal conductivity prediction of materials using machine learning potential. The influence of the hydroparameters of two cutoff radii in NEP models on reproduced energy and force, structure features, computational efficiency and spectral thermal conductivity was systematically analyzed and the optimized cutoff radius of 4.5 Å achieves a balance between computational efficiency and accuracy. Furthermore, the force prediction error correction method of NEP models effectively reduces the error arising from the additional force noise in the Langevin thermostat by extrapolating to the zero-force error limit. This study provides valuable insights and hold significant implication for advacing efficient thermal management technologies in wide-bandgap semiconductor devices.

Acknowledgement

This work was supported by the National Natural Science Foundation of China (No. 52376063 and No 52306116), the Hebei Key Laboratory of Low Carbon and High Efficiency Power Generation Technology Prevention Fund (Grant No. 2022-K03) and the China Postdoctoral Science Foundation (No. 2023MD744223).

References

- 1 J. P. Kozak, R. Zhang, M. Porter, Q. Song, J. Liu, B. Wang, R. Wang, W. Saito, and Y. Zhang, *IEEE Transactions on Power Electronics* **38** (7), 8442 (2023).
- 2 Koon Hoo Teo, Yuhao Zhang, Nadim Chowdhury, Shaloo Rakheja, Rui Ma, Qingyun Xie, Eiji Yagyu, Koji Yamanaka, Kexin Li, and TomC s Palacios, *Journal of Applied Physics* **130** (16), 160902 (2021).
- 3 Yuan Qin, Benjamin Albano, Joseph Spencer, James Spencer Lundh, Boyan Wang, Cyril Buttay, Marko Tadjer, Christina DiMarino, and Yuhao Zhang, *Journal of Physics D: Applied Physics* **56** (9), 093001 (2023).
- 4 Mohd Faizol Abdullah, Mohd Rofei Mat Hussin, Muhamad Amri Ismail, and Sharaifah Kamariah Wan Sabli, *Microelectronic Engineering* **273**, 111958 (2023).
- 5 L. Lindsay, D. A. Broido, and T. L. Reinecke, *Physical Review Letters* **109** (9), 095901 (2012).
- 6 Atsushi Togo, Laurent Chaput, and Isao Tanaka, *Physical Review B* **91** (9), 094306 (2015).
- 7 Dao-Sheng Tang, Guang-Zhao Qin, Ming Hu, and Bing-Yang Cao, *Journal of Applied Physics* **127** (3), 035102 (2020).
- 8 C. Mion, J. F. Muth, E. A. Preble, and D. Hanser, *Applied Physics Letters* **89** (9), 092123 (2006).
- 9 Roland B. Simon, Julian Anaya, and Martin Kuball, *Applied Physics Letters* **105** (20), 202105 (2014).
- 10 Robert Rounds, Biplab Sarkar, Tomasz Sochacki, Michal Bockowski, Masayuki Imanishi, Yusuke Mori, Ronny Kirste, RamC n Collazo, and Zlatko Sitar, *Journal of Applied Physics* **124** (10), 105106 (2018).
- 11 Qiye Zheng, Chunhua Li, Akash Rai, Jacob H. Leach, David A. Broido, and David G. Cahill, *Physical Review Materials* **3** (1), 014601 (2019).

- 12 Ruikang Wu, Run Hu, and Xiaobing Luo, *Journal of Applied Physics* **119** (14), 145706 (2016).
- 13 Jianshi Sun, Shouhang Li, Zhen Tong, Cheng Shao, Xiangchuan Chen, Qianqian Liu, Yucheng Xiong, Meng An, and Xiangjun Liu, *Physical Review B* **109** (13), 134308 (2024).
- 14 X. W. Zhou, S. Aubry, R. E. Jones, A. Greenstein, and P. K. Schelling, *Physical Review B* **79** (11), 115201 (2009).
- 15 Zhi Liang, Ankit Jain, Alan J. H. McGaughey, and Pawel Koblinski, *Journal of Applied Physics* **118** (12), 125104 (2015).
- 16 Pavel Korotaev, Ivan Novoselov, Aleksey Yanilkin, and Alexander Shapeev, *Physical Review B* **100** (14), 144308 (2019).
- 17 X. Qian, S. Peng, X. Li, Y. Wei, and R. Yang, *Materials Today Physics* **10**, 100140 (2019).
- 18 Zheyong Fan, Zezhu Zeng, Cunzhi Zhang, Yanzhou Wang, Keke Song, Haikuan Dong, Yue Chen, and Tapio Ala-Nissila, *Physical Review B* **104** (10), 104309 (2021).
- 19 Giovanni Bussi and Michele Parrinello, *Physical Review E* **75** (5), 056707 (2007).
- 20 D. C. vid P. C. ter KovC!cs, Ilyes Batatia, Eszter S. C. ra Arany, and G. C. bor CsC!nyi, *The Journal of Chemical Physics* **159** (4), 044118 (2023).
- 21 Ask Hjorth Larsen, Jens Jørgen Mortensen, Jakob Blomqvist, Ivano E. Castelli, Rune Christensen, Marcin Dułak, Jesper Friis, Michael N. Groves, Bjørk Hammer, Cory Hargus, Eric D. Hermes, Paul C. Jennings, Peter Bjerre Jensen, James Kermode, John R. Kitchin, Esben Leonhard Kolsbjerg, Joseph Kubal, Kristen Kaasbjerg, Steen Lysgaard, Jón Bergmann Maronsson, Tristan Maxson, Thomas Olsen, Lars Pastewka, Andrew Peterson, Carsten Rostgaard, Jakob Schiøtz, Ole Schütt, Mikkel Strange, Kristian S. Thygesen, Tejs Vegge, Lasse Vilhelmsen, Michael Walter, Zhenhua Zeng, and Karsten W. Jacobsen, *Journal of Physics: Condensed Matter* **29** (27), 273002 (2017).
- 22 G. Kresse and FurthmC, *Physical Review B* **54** (16), 11169 (1996).
- 23 John P. Perdew, Kieron Burke, and Matthias Ernzerhof, *Physical Review Letters* **77** (18), 3865 (1996).
- 24 Koichi Momma and Fujio Izumi, *Journal of Applied Crystallography* **41** (3), 653 (2008).
- 25 Zheyong Fan, Yanzhou Wang, Penghua Ying, Keke Song, Junjie Wang, Yong Wang, Zezhu Zeng, Ke Xu, Eric Lindgren, J. Magnus Rahm, Alexander J. Gabourie, Jiahui Liu, Haikuan Dong, Jianyang Wu, Yue Chen, Zheng Zhong, Jian Sun, Paul Erhart, Yanjing Su, and Tapio Ala-Nissila, *The Journal of Chemical Physics* **157** (11), 114801 (2022).
- 26 Keke Song, Rui Zhao, Jiahui Liu, Yanzhou Wang, Eric Lindgren, Yong Wang, Shunda Chen, Ke Xu, Ting Liang, Penghua Ying, Nan Xu, Zhiqiang Zhao, Jiuyang Shi, Junjie Wang, Shuang Lyu, Zezhu Zeng, Shirong Liang, Haikuan Dong, Ligang Sun, Yue Chen, Zhuhua Zhang, Wanlin Guo, Ping Qian, Jian Sun, Paul Erhart, Tapio Ala-Nissila, Yanjing Su, and Zheyong Fan, *Nature Communications* **15** (1), 10208 (2024).
- 27 Mattia Bernetti and Giovanni Bussi, *The Journal of Chemical Physics* **153** (11), 114107 (2020).
- 28 Giovanni Bussi, Davide Donadio, and Michele Parrinello, *The Journal of Chemical Physics* **126** (1), 014101 (2007).
- 29 Zheyong Fan, Haikuan Dong, Ari Harju, and Tapio Ala-Nissila, *Physical Review B* **99** (6), 064308 (2019).
- 30 Yanzhou Wang, Zheyong Fan, Ping Qian, Miguel A. Caro, and Tapio Ala-Nissila, *Physical Review B* **107** (5), 054303 (2023).
- 31 Penghua Ying and Zheyong Fan, *Journal of Physics: Condensed Matter* **36** (12), 125901 (2024).
- 32 Juan Xue, Fengyi Li, Aoran Fan, Weigang Ma, and Xing Zhang, *International Journal of Heat and Mass Transfer* **233**, 126049 (2024).

- 33 Xiguang Wu, Wenjiang Zhou, Haikuan Dong, Penghua Ying, Yanzhou Wang, Bai Song, Zheyong Fan, and Shiyun Xiong, *The Journal of Chemical Physics* **161** (1), 014103 (2024).
- 34 Wenjiang Zhou, Nianjie Liang, Xiguang Wu, Shiyun Xiong, Zheyong Fan, and Bai Song, *Materials Today Physics* **50**, 101638 (2025).